β-Si₃N₄ Microcrystals Prepared by Carbothermal Reduction-Nitridation of Quartz

Meng Zhang [1] , **Zhi Chen** [1] , **Juntong Huang** [1,*], **Saifang Huang** [2], **Zhihui Hu** [1], **Zhijun Feng** [1], **Qingming Xiong** [1] **and Xibao Li** [1,*]

[1] School of Materials Science and Engineering, Nanchang Hangkong University, Nanchang 330063, Jiangxi Province, China; zhangmeng4747@163.com (M.Z.); chenzhi_2018@126.com (Z.C.); Huzhihui94@163.com (Z.H.); fengzhijun@nchu.edu.cn (Z.F.); xiongqingming123@163.com (Q.X.)

[2] Department of Chemical and Materials Engineering, University of Auckland, Private Bag 92019, Auckland 1142, New Zealand; shua084@aucklanduni.ac.nz

* Correspondence: huangjt@nchu.edu.cn (J.H.); lixibao@nchu.edu.cn (X.L.); Tel./Fax: +86-791-83863732 (J.H.)

check for updates

Abstract: Single phase β-Si₃N₄ with microcrystals was synthesized via carbothermal reduction-nitridation (CRN) of quartz and carbon coke powder as starting materials. The effects of reaction parameters, i.e., heating temperature, holding time, C/SiO₂ ratio, Fe₂O₃ additive and β-Si₃N₄ seeds on the phase transformation and morphology of products were investigated and discussed. Rather than receiving a mixture of both α- and β- phases of Si₃N₄ in the products, we synthesized powders of β-Si₃N₄ single polymorph in this work. The mechanism for the CRN synthesis of β-Si₃N₄ from quartz and the formation mechanism of Fe₃Si droplets were discussed. We also firstly reported the formation of Fe₃Si Archimedean solids from a CRN process where Fe₂O₃ was introduced as additive. Comparing to the gear-like short columnar morphology observed in samples without β-Si₃N₄ seeding, the addition of β-Si₃N₄ seeds led to an elongated morphology of final products and much finer widths. In addition, the β-Si₃N₄ microcrystals exhibited a violet-blue spectral emission range, which could be highly valuable for their future potential optoelectronic applications.

Keywords: β-Si₃N₄ microcrystals; Fe₃Si archimedean solids; quartz; carbothermal reduction nitridation; seeding

1. Introduction

Silicon nitride (Si₃N₄) is an important high temperature structural material because of its excellent properties, including high strength, high decomposition temperature (1900 °C), good resistance to oxidation, thermal shock, corrosive environments, which have been investigated extensively over the past three decades [1–4].

The most prevalent methods for preparing Si₃N₄ powders include direct nitridation method, carbothermal reduction-nitridation (CRN) method and thermal decomposition method [5–7]. By CRN method, Si₃N₄ powders or columnar grains with excellent size distribution and physical properties could be synthesized and used as thermal conductive fillers or commercial applications for manufacturing engineering devices [8,9]. For example, Karakus et al. [9]. synthesized α-Si₃N₄ powders by CRN of synthetic silica and activated charcoal at 1470 °C, and then used the obtained α-Si₃N₄ powders as the raw materials to prepare the Si₃N₄ ceramic by a pressureless sintering method. Comparing the results with commercial Si₃N₄ powders, the resultant Si₃N₄ powders by CRN method indicated a similar or ever better density and β-phase conversion by the pressureless sintering. Yin et al. prepared ZrN–Si₃N₄ composite powders from natural zircon and quartz via CRN reaction at temperatures below 1600 °C [10]. Similarly, Arik prepared Si₃N₄ powders by CRN from diatomite

with C/SiO$_2$ molar ratio 4 at 1400 °C for 16 h [11]. Thus, it is feasible to prepare Si$_3$N$_4$ with quartz and carbon black. On the other hand, CRN method takes advantage from low-cost starting materials [8,9]. The high cost of raw materials is a primary limitation for large scale production of Si$_3$N$_4$ powders. Through the CRN method, it is possible to synthesize Si$_3$N$_4$ powders from low-cost quartz with abundant reserves in the world. It was reported that the same problem for the massive production of SiC powders was overcome by this way, and the product was much finer for achieving excellent flexural strength [12].

Grain size and shape of Si$_3$N$_4$ powders can influence some properties of Si$_3$N$_4$-based products such as varying electrical and optical properties and mechanical properties [13,14]. Apart from Si$_3$N$_4$ seeds, Fe and its oxides have been used as additives to change the morphology of a product or to promote nitriding process [15–18]. However, to the best of our knowledge, the crystal microstructure/morphology of Fe-containing compounds formed in the nitridation process while Fe or iron oxide being used as additive was rarely reported.

In this study, quartz and carbon coke powders were selected as raw materials to prepare Si$_3$N$_4$ powders via CRN method. The influence of temperature, holding times, C/SiO$_2$ molar ratio, additive amount of Fe$_2$O$_3$ and β-Si$_3$N$_4$ seeds were studied on the phase transformation and morphology of products. Faceted Fe$_3$Si Archimedean solids, a novel morphology of the iron silicide, were observed firstly which have the potential application in spintronics devices [19]. The formation mechanism of products from the nitridation reaction was discussed and photoluminescence (PL) properties of samples were also detected.

2. Experimental

2.1. Materials

Natural quartz powders (granularity ≤ 400 mesh, chemical composition (wt.%): SiO$_2$: 97.8, Al$_2$O$_3$: 0.63, Fe$_2$O$_3$: 0.13, CaO: 0.08, K$_2$O: 0.05, others: 1.31), and coke powders (granularity ≤ 200 mesh, carbon content = 88%) were used as the main starting raw materials. The crystalline phase of the natural quartz powders was hexagonal α-quartz (Figure 1). Fe$_2$O$_3$ (A.R. grade, Sinopharm Chemical Reagent Beijing Co., Ltd., Beijing, China) and Si$_3$N$_4$ (A.R. grade, ~800 nm, Shanghai Pantian powder material Co., Ltd., Shanghai, China) were used as additives. The starting compositions of all the samples are listed in Table 1.
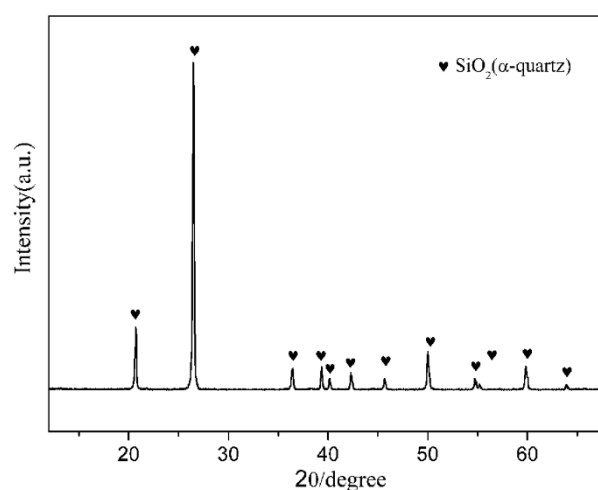

Figure 1. X-ray diffraction (XRD) pattern of natural quartz.

Table 1. Compositional design of the samples (wt.%).

Samples	C/SiO$_2$ Molar Ratio	Coke	Quartz	Fe$_2$O$_3$ (Extra)	β-Si$_3$N$_4$ (Extra)
S1	2	30.77	69.23	0	0
S2	2.2	32.84	67.16	0	0
S3	3	40.00	60.00	0	0
S4	4	47.06	52.94	0	0
S5	2	30.77	69.23	4	0
S6	2	30.77	69.23	0	2

2.2. Methods

The starting materials were ball-milled together for 2 h. Then, 2 g of the mixed powders were die-pressed under 20 MPa into a specimen of 10 mm in diameter. The specimens were placed in a graphite crucible and heated in flow nitrogen (purity 99.999%) in the reaction chamber of a tube furnace at temperatures in the range of 1450–1600 °C. A two stage heating schedule was used, i.e., heating up from ambient temperature to 1000 °C at 10 °C·min^{-1}, then raising to the final temperature at 5 °C·min^{-1} and held for 3 h. The final temperatures were set as 1470 °C, 1500 °C, 1530 °C, 1550 °C, 1570 °C, and 1600 °C, respectively. In addition, in order to study the effect of holding time to the CRNed product, S1 sample was synthesized at 1600 °C and held for 1 h, 2 h, and 3 h, respectively. The fired samples were furnace-cooled to room temperature, and then reheated in air at 700 °C for 2 h to remove the residual carbon.

2.3. Characterization

The crystalline phases of the synthesized products were identified by X-ray diffraction (XRD; D8 Advance diffractometer, Bruker, Rheinstetten, Germany), using Cu Kα_1 radiation (λ = 1.5406 Å) with a step of 0.02° (2θ) and a scanning rate of 4° min^{-1}. The microstructures and morphologies of the products were observed by scanning electron microscopy (SEM; JEM-6460LV microscope, JEOL, Tokyo, Japan) and high-resolution transmission electron microscopy (HRTEM, JEM2010, JEOL, Tokyo, Japan). The energy dispersive X-ray spectroscopies (EDS) linked with the SEM and the HRTEM were employed to assist the micro-area chemical analysis of the products. FT-IR spectra were collected at room temperature using a FT-IR Spectrometer (FT/IR-4000 JASCO, Tokyo, Japan) equipped with a Michelson 28° interferometer with corner-cube mirrors, covering a range between 250,000 and 5 cm^{-1}. Photoluminescence emission (PL) spectra were measured by F-7000 fluorescence spectrophotometer (Eppendorf, Shanghai, China) with a photomultiplier tube functioning at 700 V, and a 150 W Xe lamp as the excitation source.

3. Results and Discussion

3.1. Influence of Synthetic Schedule on the Phase Composition and Morphology of Products

3.1.1. Influence of Temperature on the Phase Composition and Morphology of Products

Figure 2 shows XRD patterns of sample S1 nitrided at different temperatures for 3 h. As can be seen, cristobalite was the dominant phase at 1470 °C, which was phase transition from quartz. In additional, some SiC, Si$_2$N$_2$O and residual quartz were present in the products (Figure 2a). With nitriding temperature being gradually elevated from 1470 °C to 1550 °C, intensity of β-SiC and Si$_2$N$_2$O diffraction peaks increased and that of cristobalite decreased (Figure 2a–d). After further increasing the temperature to 1570 °C, β-Si$_3$N$_4$ had just emerged while its diffraction intensity was much lower than that of β-SiC and Si$_2$N$_2$O; in the meantime, the peaks of cristobalite disappeared, and no other silica phases were detected (Figure 2e). By applying a higher temperature of 1600 °C, β-Si$_3$N$_4$ was formed in a relatively high purity (Figure 2f). The intensity of the secondary phase β-SiC was very weak. The

β-Si$_3$N$_4$ synthesized at 1570 & 1600 °C (Figure 2e,f) in S1 crystallized as a hexagonal structure and their lattice parameters and cell volumes are listed in Table 2. They were increased from 1570 to 1600 °C. The weight fraction of each phase in S1 at 1570 & 1600 °C is shown Table 3, the weight fraction was remarkable increased from 32.30 to 91.52 with the increased of temperature to 1600 °C. Upon the above observation, it is clear that in this work, the effect of temperature on the phase formation from quartz by CRN is very significant. For the holding period of 3 h, the temperature 1570 °C was critical for the transformation of cristobalite into Si$_3$N$_4$, whereas it cannot be formed at a lightly lower temperature of 1550 °C. Moreover, a temperature of 1600 °C, 30 °C higher than 1570 °C contributed to the formation of high-purity Si$_3$N$_4$ powders.
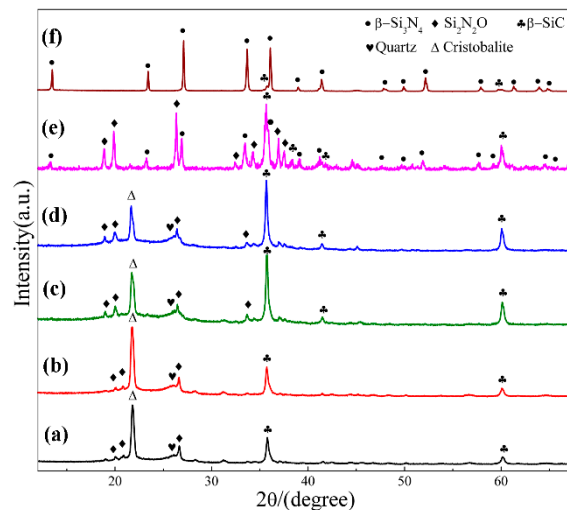

Figure 2. XRD patterns of sample S1 nitrided at different temperatures for 3 h: (**a**) 1470 °C; (**b**) 1500 °C; (**c**) 1530 °C; (**d**) 1550 °C; (**e**) 1570 °C; (**f**) 1600 °C.

Table 2. Lattice parameters and cell volume of β-Si$_3$N$_4$ in S1 & S5.

Samples	Littice Parameters		Cell Volume(Å^3)
	a(Å) = b(Å)	c(Å)	
S1, 1570 °C, Figures 2e and 7c	7.6351	2.8867	145.7343
S1, 1600 °C, Figures 2f and 7e	7.8607	2.9139	155.9293
S5, 1570 °C, Figure 7d	7.7205	2.8695	148.1248
S5, 1600 °C, Figure 7f	7.7753	2.8993	151.7952

Table 3. Weight fraction of each phase in S1 and S5 at 1570 and 1600 °C (wt. %).

Samples	β-Si$_3$N$_4$	SiC	Si$_2$N$_2$O	Fe$_3$Si
S1, 1570 °C, Figures 2e and 7c	32.20	36.06	31.74	0
S1, 1600 °C, Figures 2f and 7e	91.52	8.48	0	0
S5, 1570 °C, Figure 7d	57.46	13.41	20.74	9.39
S5, 1600 °C, Figure 7f	85.47	6.85	4.22	3.46

Morphological variation of sample S1 after being nitrided at different nitriding temperatures was investigated by SEM observation, and the elemental composition was performed by EDS analysis (Figure 3). There were many independent SiO$_2$ particles with size of 20 μm, covered by some Si$_2$N$_2$O and SiC fibers at temperatures of 1500–1550 °C, confirmed by EDS (Figure 3a–d). Some Fe element in the fibers was detected in the EDS, which should be from original quartz raw material (Figure 3e,f). In the sample synthesized at 1600 °C, short columnar grains with diameters of about 2 μm were dominant throughout the sample, which is the typical morphology of β-phase Si$_3$N$_4$. The trace amounts of Al and O was detected in the grains; this might come from impurity of original quartz or ball milling.
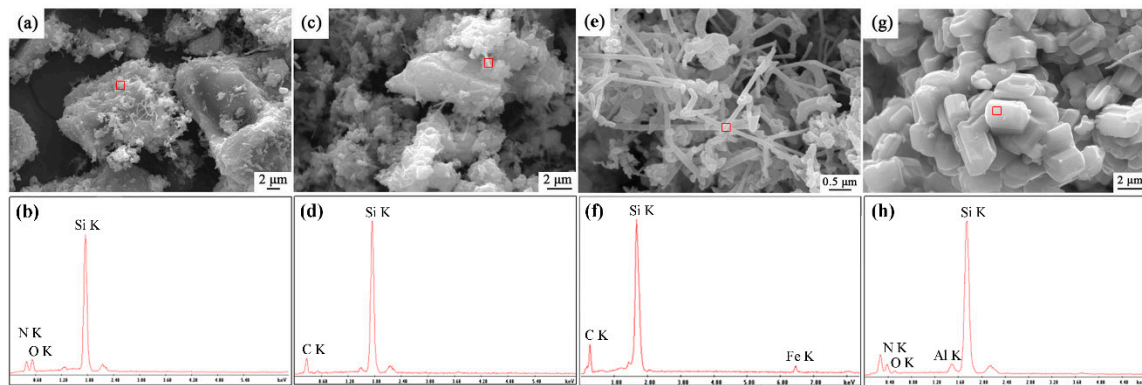
Figure 3. SEM images and X-ray spectroscopies (EDS) patterns of sample S1 nitrided at different temperatures for 3 h: (**a**,**b**) 1500 °C, (**c**,**d**) 1550 °C, (**e**,**f**) 1570 °C (**g**,**h**) 1600 °C.

3.1.2. Influence of Holding Time on the Phase Composition of Products

In order to elucidate the effect of holding time, the samples synthesized at 1600 °C for different holding times were compared. Figure 4a–c present the digital photos of three samples, which clearly demonstrated the degree of nitridation from the change in the nitridized area. As seen from the digital photos, 2 h was insufficient for CRN of quartz at 1600 °C. There were two different zones on the cross section of products (Figure 4a,b). The interior portion of pellets had a darker color while the exterior part was greenish gray. Interior regions of product narrowed down when holding time was 2 h and disappeared when 3 h. A longer holding time of 3 h enabled the complete nitridation of the entire pellet with diameter of <10 mm. The XRD patterns of them are depicted in Figure 4d,f. It is revealed that phase compositions were Si_3N_4, SiC, and Si_2N_2O for exterior region as well as SiC and Si_3N_4 for interior region with holding time of 1 h (Figure 4d,e). The diffraction peaks of SiC in interior region were evidently weakened with increasing the holding time to 2 h (Figure 4f) even almost disappeared after 3 h (Figure 2f). Since the permeation of N_2 in samples was from outside to inside, the external N_2 of samples was more abundant than that of internal. Increasing holding time allowed complete penetration of N_2 into the inner pellets, leading to the fully nitridation of the entire pellets.
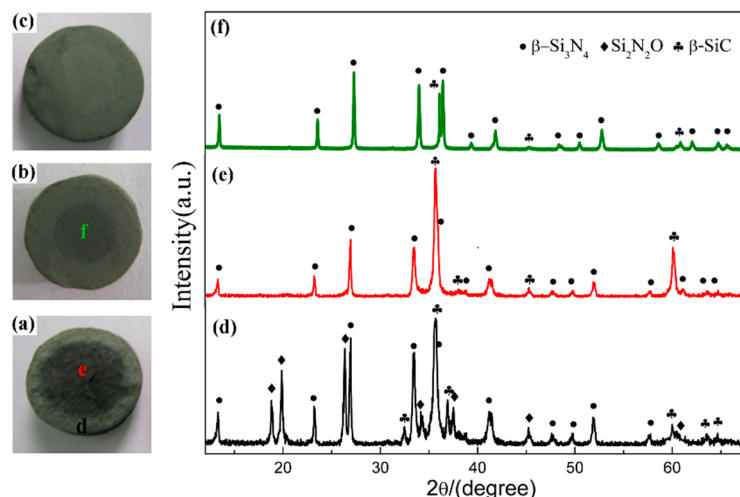

Figure 4. Digital photos of sample S1 nitrided at 1600 °C with different holding time: (**a**) 1 h, (**b**) 2 h, (**c**) 3 h; and XRD patterns of sample S1 in different regions: (**d**) exterior region and (**e**) interior region of pellet reacted for 1 h, (**f**) interior region of the pellet reacted for 2 h.

3.1.3. The CRN Mechanism of Quartz

Based on the results described above and literatures reported previously [20,21], it is generally accepted that the CRN reaction of quartz would happen through several steps. The reduction of quartz into SiO, via the pathways as shown by Equation (1) (ΔG is the Gibbs free energy of reaction, and T is the temperature), is the first but a critical step, which enables the further reduction process.

$$SiO_2(s) + C(s) \rightarrow SiO(g) + CO(g), \Delta G = 665.578\text{-}0.33T \text{ kJ/mol} \tag{1}$$
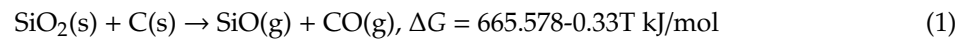
The as-reduced SiO (g) is then nitrided into silicon nitride phases by carbon through the Equation (2) [22,23].

$$3SiO(g) + 3C(s) + 2N_2(g) \rightarrow Si_3N_4(s) + 3CO(g), \Delta G = -830.44 + 0.35T \text{ kJ/mol} \tag{2}$$
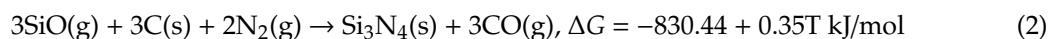
At a temperature of 1550 °C or lower, intermediate phases Si_2N_2O and SiC were preferably formed through Equations (3) and (4), respectively [22,24]. It suggests that under the subcritical temperatures (1470 to 1550 °C), the reaction process was dominated by the reductive atmosphere/conditions while the nitridation processes were less thermodynamically preferred.
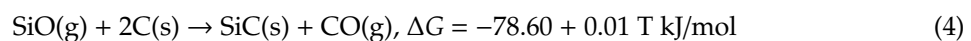
$$2SiO_2(s) + 3C(s) + N_2(g) \rightarrow Si_2N_2O(s) + 3CO(g), \Delta G = 572.54\text{-}0.32T \text{ kJ/mol} \tag{3}$$

$$SiO(g) + 2C(s) \rightarrow SiC(s) + CO(g), \Delta G = -78.60 + 0.01 \text{ T kJ/mol} \tag{4}$$

Figure 5 is a schematic diagram demonstrating the synthesis of β-Si_3N_4 by CRN of quartz in two major steps. As the first step, illustrated by Figure 5a–c, SiO(g) forms via Equation (1) beyond certain temperature. Equation (1) requires direct contact of carbon and SiO_2. Then in the next step, as shown in Figure 5d, Si_3N_4 nucleates from Equation (2), and grows up on the surface of carbon and SiO_2, which is associated with the diffusion rate of SiO. The reaction process is progressive from exterior to interior of the sample pellets as shown in Figure 5f.
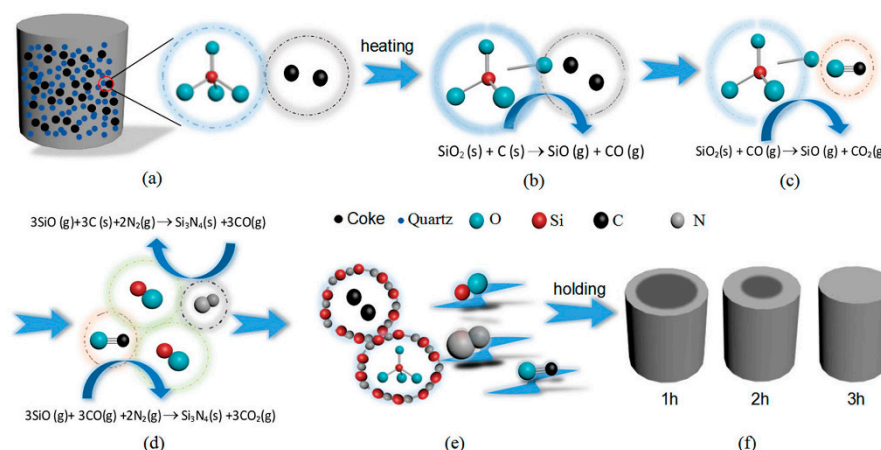

Figure 5. Reaction schematic diagram for the formation of β-Si_3N_4 by carbothermal reduction-nitridation (CRN) of quartz: (**a**) the green body of specimen, (**b–e**) nitridation processes of raw materials, (**f**) specimens obtained under different holding times.

3.2. Influences of Starting Composition and Additive on Phase Composition and Morphology of Products

In order to elucidate the key factors for the synthesis of β-phase Si_3N_4 from quartz CRN synthesis, we investigated the effects of C/SiO_2 molar ratio, Fe_2O_3 additive content, and the introduction of β-Si_3N_4 seeds on the products.

3.2.1. Influence of C/SiO$_2$ Molar Ratio on Phase Composition

According to Equation (5), the theoretical C/SiO$_2$ molar ratio of Si$_3$N$_4$ is 2 [25]. Thus, samples S1–S4 with different C/SiO$_2$ molar ratios (2, 2.2, 3, and 4) were designed and subjected to CRN synthesis at 1600 °C for 3 h.
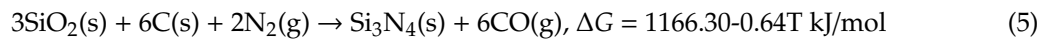
$$3SiO_2(s) + 6C(s) + 2N_2(g) \rightarrow Si_3N_4(s) + 6CO(g), \Delta G = 1166.30\text{-}0.64T \text{ kJ/mol} \tag{5}$$

Figure 6 shows the XRD patterns of samples S1~S4 nitrided at 1600 °C for 3 h. As seen in the figure, β-Si$_3$N$_4$ was the main phase when C/SiO$_2$ was 2 (sample S1) and 2.2 (Sample S2), with trace amount of β-SiC. Peaks of β-Si$_3$N$_4$ decreased significantly when a higher C/SiO$_2$ molar ratio of 3 was adopted in sample S3, and almost disappeared when the C/SiO$_2$ ratio further increased to 4 (sample S4). At the meantime, β-cristobalite was detected which was derived from the phase transformation of residual quartz at high temperature. The results indicate that the theoretical/stoichiometric carbon content as per Equation (5) was optimal for preparing single-phase β-Si$_3$N$_4$ from quartz by CRN. Increased amount of β-SiC and other by-products formed in the product of samples with a higher C/SiO$_2$ molar ratio.
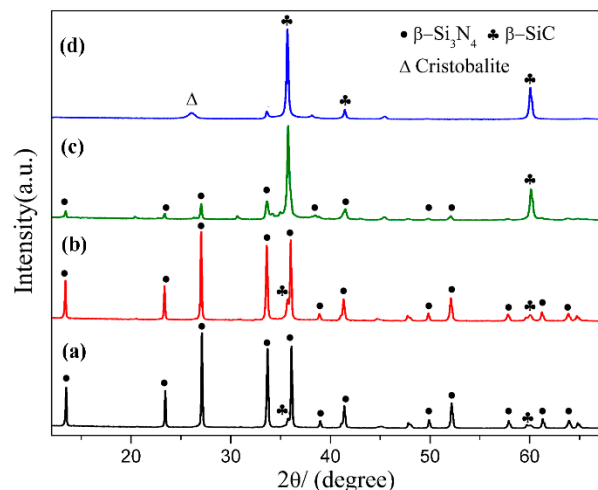

Figure 6. XRD patterns of sample S1~S4 nitrided at 1600 °C for 3 h: (**a**) S1, C/SiO$_2$ = 2; (**b**) S2, C/SiO$_2$ = 2.2; (**c**) S3, C/SiO$_2$ = 3; (**d**) S4, C/SiO$_2$ = 4.

3.2.2. Influence of Fe$_2$O$_3$ Additive on Phase Composition and Morphology of Products

In order to see the effect of additive, we designed a composition (sample S5) which added extra 4 wt.% Fe$_2$O$_3$ into the starting mixture. The XRD patterns of sample S1 (Fe$_2$O$_3$-free) and S5 (with extra 4 wt.% Fe$_2$O$_3$) are plotted in Figure 7, where the phase assemblages in the samples at different temperatures are compared. At 1470 °C, β-cristobalite, quartz and β-SiC were the main phases in sample S1. In contrast, much weaker peaks of cristobalite showed in sample S5 whereas Si$_2$N$_2$O and β-Si$_3$N$_4$ formed with a considerable amount. At 1570 °C, β-Si$_3$N$_4$, β-SiC and Si$_2$N$_2$O were present in both sample S1 and sample S5, while there was significantly more β-Si$_3$N$_4$ and much less β-SiC formed in sample S5 (comparing to S1). At 1600 °C, both samples had β-Si$_3$N$_4$ as dominant phase and trace amount of β-SiC, and the trace amount of Si$_2$N$_2$O were found in S5. Additionally, peaks appeared at 45.5° in sample S5 at all temperatures can be assigned to Fe$_3$Si. The parameters and cell volumes of β-Si$_3$N$_4$ synthesized in S1 and S5 at 1600 °C (Figure 7e,f) are listed in Table 2. Table 3 is the weight fraction of each phase in S1 and S5 at 1570 and 1600 °C. These results illustrate that Fe$_2$O$_3$ could enhance the carbothermal reduction process of quartz and nitridation transformation to β-Si$_3$N$_4$.
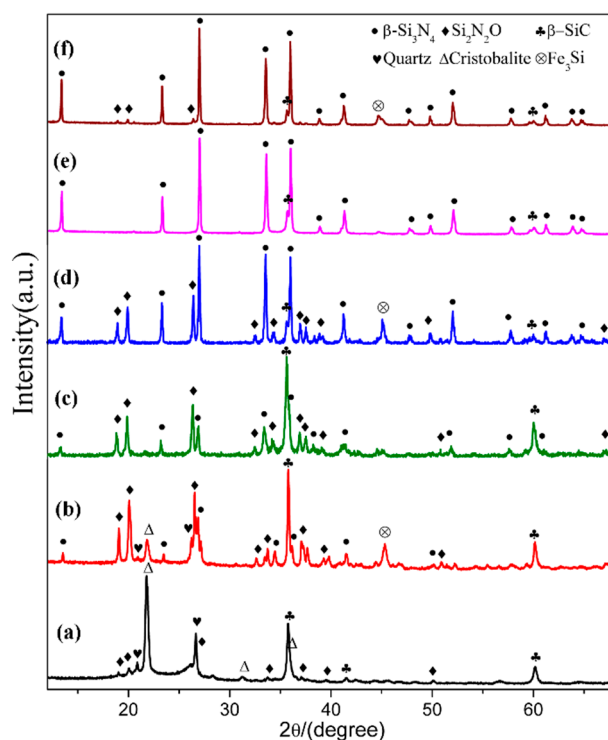
Figure 7. XRD patterns of sample S1(**a**,**c**,**e**), and sample S5 (**b**,**d**,**f**) at 1470, 1570, and 1600 °C, respectively.

Figure 8 shows the SEM images and EDS results of sample S5 nitrided at 1600 °C. As seen in Figure 8a–d, the columnar grains had gear-like morphologies and dominate in the products, which could be assigned to β-Si$_3$N$_4$ upon XRD and EDS results. A trace amount of Fe element was detected (Figure 8f), which was originated from the additive added in this sample. Furthermore, a white-colored product layer was covered on the surface of sample S5 nitrided at 1600 °C for 3 h. SEM observation shows that it was composed of fibers with widths of about 0.3–0.5 μm (Figure 9a,b). EDS result reveals that the fibers were SiC phase (Figure 9d). At the tip of each fiber, there was a spherical particle containing Si-Fe-O elements (Figure 9a,c). It is therefore suggested that the SiC fibers formed through a Vapor - Liquid - Solid (VLS) mechanism [26].
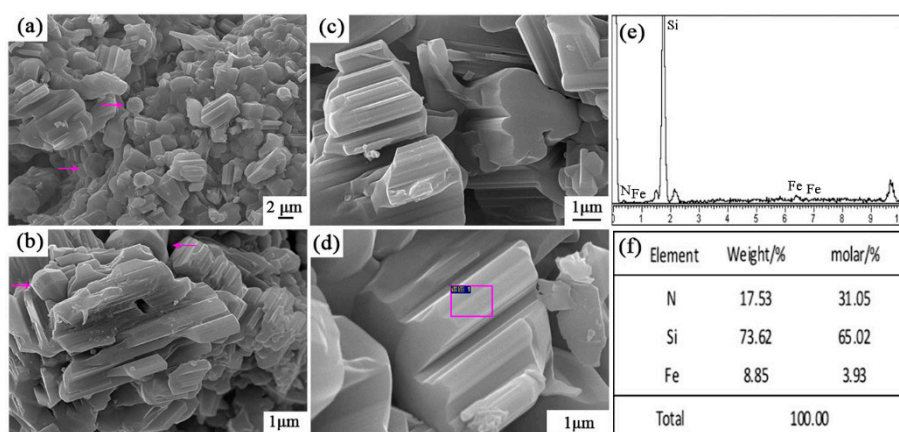

Figure 8. SEM images and EDS patterns of β-Si$_3$N$_4$ in sample S5 nitrided at 1600 °C: (**a**–**d**) SEM images with different magnification, (**e**,**f**) EDS results of the selected area in (**d**).
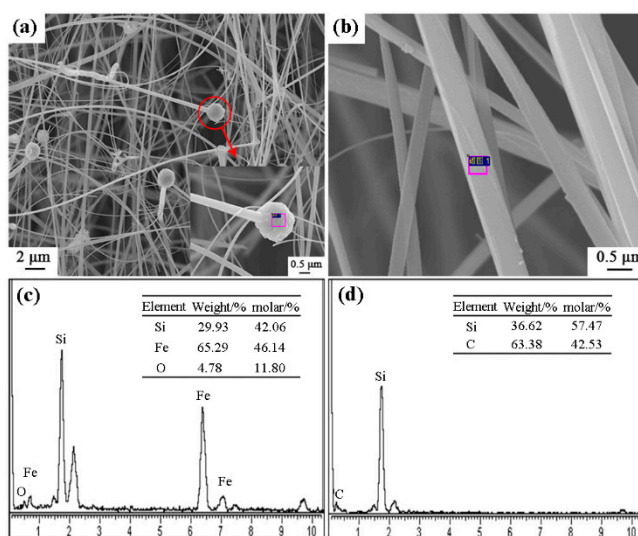
Figure 9. SEM images and EDS patterns of SiC fibers on the surface of sample S5 nitrided at 1600 °C: (**a**,**b**) SEM images of white-colored product layer, (**c**,**d**) EDS results of the selected area in (**a**,**b**).

Very interestingly, some spherical particles were observed in sample S5 (arrowed in Figure 8a,b), which were further characterized by SEM and EDS (Figure 10). It is wonderful to see that they were Archimedean solids with sizes of several microns. EDS results illustrate that they contained only Fe and Si elements with the molar ratio of Fe/Si ~2.79. This result clearly reveals that the faceted crystal was Fe_3Si as detected in XRD data. To the best of our knowledge, such a novel morphology of Fe_3Si was never reported in the literature.
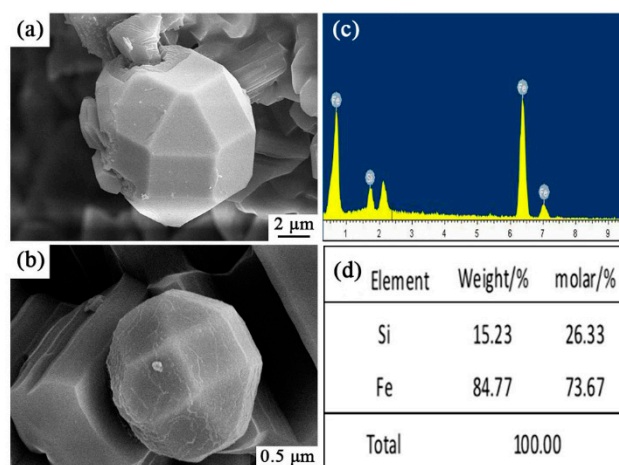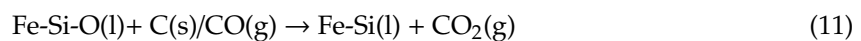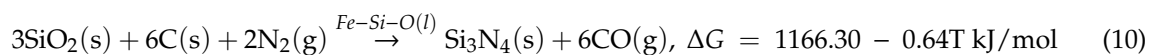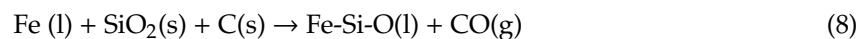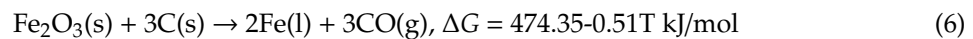

Figure 10. SEM images and EDS patterns of Si-Fe alloy of sample S5 nitrided at 1600 °C: (**a**,**b**) SEM images of spherical particles in sample S5, (**c**,**d**) EDS results of the selected area in (**a**,**b**).

Based on the above results, it can be concluded that Fe_2O_3 had a remarkable catalytic effect on the CRN of quartz at a lower temperature than 1600 °C. Under the reductive environment at high temperatures, carbon or CO can reduce Fe_2O_3 to Fe by Equations (6) or (7). It is known that the melting point of pure iron is 1538 °C. Therefore, Fe generally attaches to a support material in the reaction system by forming a liquid phase. In the present study, we speculate that Fe-Si-O liquid formed first (Equation (8), Figure 9). The Fe-containing liquid could dissolve SiO_2 and C, then enhance their reaction to form SiO(g) [27] (Equation (9)), consequently promoting the formation of Si_2N_2O, SiC and even β-Si_3N_4 at lower temperature (Equations (3) and (4), Figure 7). Fe-containing liquid could significantly enhance the nitridation reaction, and the precipitation of β-Si_3N_4 has been known

to be favored by the presence of Fe-containing liquid [28] (Equation (10)). Fe-Si-O liquids were further reduced to be Fe-Si containing liquid (Equation (11)). The Fe-rich liquid then crystallized as Fe_3Si crystals while cooling (Equation (12)). The Fe-containing liquid phases, as a catalytic phase, promoted the formation of Si_3N_4, which is clearly illustrated by the phase assemblages in the samples at the low temperatures (Figure 5). Nevertheless, it is yet unclear how the unique Archimedean solids formed, which is beyond the objectives of this work and needs further investigation in near future.

$$Fe_2O_3(s) + 3C(s) \rightarrow 2Fe(l) + 3CO(g), \Delta G = 474.35\text{-}0.51T \text{ kJ/mol} \tag{6}$$

$$Fe_2O_3(s) + 3CO(g) \rightarrow 2Fe(l) + 3CO_2(g), \Delta G = -6.32\text{-}0.01T \text{ kJ/mol} \tag{7}$$

$$Fe\,(l) + SiO_2(s) + C(s) \rightarrow Fe\text{-}Si\text{-}O(l) + CO(g) \tag{8}$$

$$SiO_2(s) + C(s) \xrightarrow{Fe-Si-O(l)} SiO(g) + CO(g), \Delta G = 665.59 - 0.33T \text{ kJ/mol} \tag{9}$$

$$3SiO_2(s) + 6C(s) + 2N_2(g) \xrightarrow{Fe-Si-O(l)} Si_3N_4(s) + 6CO(g), \Delta G = 1166.30 - 0.64T \text{ kJ/mol} \tag{10}$$

$$Fe\text{-}Si\text{-}O(l) + C(s)/CO(g) \rightarrow Fe\text{-}Si(l) + CO_2(g) \tag{11}$$

$$Fe\text{-}Si(l) \rightarrow Fe_3Si(s) \tag{12}$$

3.2.3. Influence of β-Si_3N_4 Seeds on Morphology of Products

The microstructure of sample S1 (no seeds) and S6 (with extra 2 wt.% Si_3N_4 seeds) synthesized at 1600 °C for 3 h were shown in Figure 11. In sample S1, the morphology of β-Si_3N_4 grains are short columnar, having grain sizes of around 3 μm. While in sample S6, grains were elongated and the gear-like morphology was rarely observed. From Figure 11c, the widths of the elongated grains are much smaller (0.2–0.5 μm) than those of short columnar grains in S1 (2–3 μm). HRTEM lattice image of the Si_3N_4 elongated grain indicates that the lattice fringe had no obvious distortion (Figure 11f,g). The measured lattice fringe spacing of 0.38 nm matched well with the (110) plane of β-Si_3N_4 (Figure 11f).
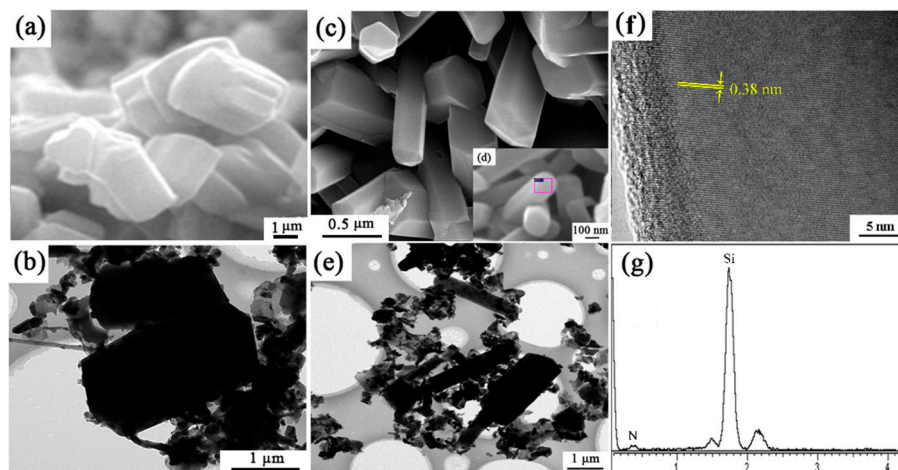

Figure 11. SEM, TEM/HRTEM images and EDS patterns of (**a,b**) sample S1 and (**c–g**) S6 nitrided at 1600 °C for 3 h.

It is reported that introducing seeds into the starting materials could affect the microstructure of synthesized products and improve the physical properties of final ceramics [29,30]. For example, in the synthesis of Sialon powders, the addition of Sialon seeds would increase the growth competition among the grains, leading to an elongated columnar morphology, thus improving flexural strength and fracture toughness [24,31]. Herein, a significantly increased aspect ratio of Si_3N_4 grains was

achieved by adding seeds into the starting mixtures. The addition of seeds could trigger heterogeneous nucleation [32]:

$$\Delta G^* = \frac{16\pi\sigma_{\alpha\beta}^3}{3\Delta g_{v_v}^2} f(\theta) = \Delta G_0^* f(\theta) \tag{13}$$

where θ is contact angle between new Si_3N_4 nucleus and Si_3N_4 seeds, $f(\theta)$ is the influence function of θ, and ΔG^* is Gibbs free energy of homogeneous nucleation. Therefore, when the contact angle was 0–180°, nucleation power could be reduced. Moreover, while crystal structure of seeds was the same as that of Si_3N_4, θ would be very small, which would reduce ΔG and make more nucleus formed at the early stage of nitriding process. Thus, the growth competition between those nuclei would made the smaller and long columnization of Si_3N_4 grains.

3.3. The Possible Mechanisms of β-Si₃N₄ Single Polymorph Formation

Usually, α- and β- Si_3N_4 polymorphs are present in the products from carbothermal reduction nitridation of SiO_2, and some related researches reported in the literature are summarized in Table 4. The phase composition ratio of α/β-Si_3N_4 in the CRN products was highly affected by additives (or impurities). For example, Sun et al. [8] reported that the yield of β-Si_3N_4 increased from 42.8% to 81.8% when improving CaF_2 additive contents (Table 4 (1 and 2)). Wang et al. [22] revealed that the introduction of CaF_2-Y_2O_3 additives significantly promoted the conversion of α-Si_3N_4 to β-Si_3N_4 (Tabele 4 (3 and 4)). Furthermore, the CRN temperature was another key factor. According to the literatures [33–35], the increasing CRN temperature was beneficial for the transformation of α-Si_3N_4 to β-Si_3N_4 (Table 4 (6 and 7), (8 and 9), (10 and 11)), and when it was higher than 1500 °C, β-Si_3N_4 emerged as the major phase, even single phase at 1700 °C (Table 4 (5)).

Table 4. Comparison of reaction conditions and products by carbothermal reduction nitridation of SiO_2 reported in the literature and the present study.

No.	Raw Materials	Carbon Source	Additive	T/°C-t/h	Products	Reference
1	Amorphous SiO_2	carbon black	CaF_2-1%	1500-2	β(42.8%) and α	[8]
2	Amorphous SiO_2	carbon black	CaF_2-10%	1500-2	β(81.8%) and α	[8]
3	Amorphous SiO_2	carbon black	None	1500-2	β(52.4%) and α	[22]
4	Amorphous SiO_2	carbon black	CaF_2, Y_2O_3	1500-2	β(90%) and α	[22]
5	Amorphous SiO_2	carbon black	CaF_2, Y_2O_3	1700-2	β(100%)	[22]
6	Quartz powder	carbon black	Y_2O_3, Bentonite	1450-3	β(26.9%), α	[34]
7	Quartz powder	carbon black	Y_2O_3, Bentonite	1500-3	β(85.7%), α	[34]
8	Synthetic silica	activated charcoal	MgO or Y_2O_3	1375-3	Si_2N_2O, β:α = 1:9	[35]
9	Synthetic silica	activated charcoal	MgO or Y_2O_3	1475-3	β:α = 1:2	[35]
10	Quartz sand	activated charcoal	$Fe(NO_3)_3$	1300-3	quartz, Si_2N_2O, β:α = 3:4	[36]
11	Quartz sand	activated charcoal	$Fe(NO_3)_3$	1540-3	β:α = 9:1	[36]
12	Quartz	coke powders	None	1470-3	cristobalite, SiC and Si_2N_2O	This article
13	Quartz	coke powders	Fe_2O_3	1470-3	SiC, Si_2N_2O, β, quartz	This article
14	Quartz	coke powders	None	1600-3	β(100%)	This article

Note: α, β: Si_3N_4.

Herein, we successfully produced β-Si_3N_4 as the single polymorph (no α- phase co-exists), either with or without Fe_2O_3 as an additive. It is widely known that the α-Si_3N_4 derives from SiO vapor while β-Si_3N_4 from liquid phase during CNR process, and also there exist phase transformation between α-Si_3N_4 and β-Si_3N_4 [34,35]. As SiO vapor always forms during the reduction process, α-Si_3N_4 can form (temporarily at least) during the CRN process. In our study, the β-Si_3N_4 as the single polymorph formed regardless of adding Fe_2O_3 or not. Thus, we speculate the following three possible reasons that lead to the formation of single β-Si_3N_4 polymorph. Firstly, the silicon source used in this work was quartz mineral rather than commercial/pure amorphous or crystalline SiO_2 powders in other literatures reported. The high temperature stability of quartz made nitriding formation process of Si_3N_4 took

place at 1570 °C in catalyst-free sample. Secondly, according to the results and discussion above, α-Si$_3$N$_4$ was metastable at high temperature. α-phase might be generated in this work, but it was converted to β-phase at such high temperature. Last, the impurities in quartz raw material including 0.13 wt.% Fe$_2$O$_3$, or the formed eutectic liquid phases, contributed to the formation of pure β-phase in products, by either promoting the α-to-β phase transformation or direct formation of β-phase. The gear-like morphology of β-Si$_3$N$_4$ should be formed via coalescence in the iron-containing liquid phase.

3.4. PL Spectrum of Synthesized β-Si$_3$N$_4$ Samples

The functional applications of Si$_3$N$_4$ had attracted increasing interest, for instance, the optical properties of Si$_3$N$_4$ films or nanostructures have been studied [36,37]. However, Si$_3$N$_4$ microcrystals had not attracted much attention in terms of their optical properties. In this context, PL emission properties (excitation at 330 nm) of β-Si$_3$N$_4$ microcrystals with different morphologies were tested by using samples S5 and S6 nitrided at 1600 °C. The PL spectra are showed in Figure 12. The spectrum of these two samples showed a board purple emission band with the maximum at 393 nm and it could be further fitted into two Guassion peaks 390 nm (3.17 eV) of purple spectral region and 441 nm (2.81 eV) of blue spectral region. It has been reported that as an indirect gap semiconductor, the luminescence of Si$_3$N$_4$ is attributed to a defect luminescence mechanism. The PL process of Si$_3$N$_4$ could be caused by the existing defect of it which including ≡Si–Si≡, =N$^-$, ≡Si^0 and ≡Si$^-$, and those were corresponding to four types of defects of Si–Si bond, N–N bond, and Si–N dangling bonds [38,39]. The experimental data may shed light on potential application of Si$_3$N$_4$ microcrystals in optical devices.
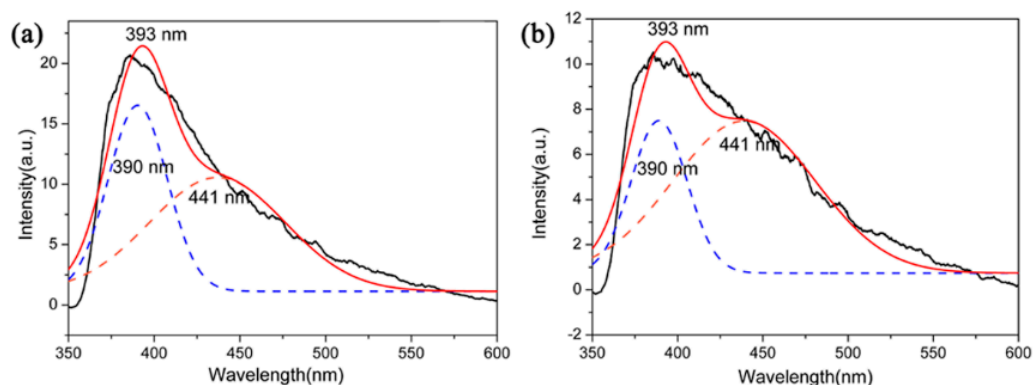

Figure 12. PL spectrum of (**a**) S5 and (**b**) S6 nitrided at 1600 °C.

4. Conclusions

A carbothermal reduction-nitridation (CRN) method was used for the preparation of β-Si$_3$N$_4$ powders from natural quartz and coke powders. β-Si$_3$N$_4$ powders with relatively high purity were obtained at 1600 °C for 3 h, with trace amount of β-SiC formed as a by-product. The results indicated that β-Si$_3$N$_4$ powders were obtained in the products, accompanied by the appearance of β-SiC and Si$_2$N$_2$O during the CRN process. The temperature, holding time, C/SiO$_2$ malor ratio, Fe$_2$O$_3$ addition, and β-Si$_3$N$_4$ seeds played important roles for the synthesis β-Si$_3$N$_4$ powders. The optimal nitriding temperature was 1600 °C and holding time was 3 h. A stoichiometric molar ratio of C/SiO$_2$ of 2 was preferred for preparing β-Si$_3$N$_4$ with better phase purity. Fe$_2$O$_3$ under the reducing environment formed Fe-containing liquid phases, which promoted the reaction thermodynamics of the CRN process. The products were mainly gear-like β-Si$_3$N$_4$ grains and Fe$_3$Si Archimedean solids. On the other hand, adding β-Si$_3$N$_4$ seeds into the starting mixture led to elongated β-Si$_3$N$_4$ grains with much finer widths and big specific ratio. The as-synthesized Si$_3$N$_4$ microcrystals exhibited an intense violet-blue spectral range with two maximum peaks at 441 nm (3.17 eV) and 390 nm (2.81 eV), which may shed light on potential application of Si$_3$N$_4$ microcrystals in optical devices.

Author Contributions: Conceptualization, J.H. and Z.C.; methodology, M.Z.; software, S.H.; validation, Z.H., Z.F. and Q.X.; formal analysis, M.Z.; investigation, X.L.; resources, J.H.; data curation, Z.C.; writing—Original draft preparation, M.Z.; writing—Review and editing, J.H.; visualization, Z.C.; supervision, J.H.; project administration, Z.H.; funding acquisition, J.H. and X.L.

Conflicts of Interest: The authors declare no conflict of interest.

References

1. Li, T.F.; Chen, Y.J.; Li, W.; Li, J.B.; Luo, L.J.; Yang, T.; Liu, L.Y.; Wu, G.L. Fabrication and mechanical properties of boron nitride nanotube reinforced silicon nitride ceramics. *Ceram. Int.* **2018**, *44*, 6456–6460. [CrossRef]

2. Huang, J.T.; Zhang, S.W.; Huang, Z.H.; Liu, Y.G.; Fang, M.H. Growth of α-Si$_3$N$_4$ nanobelts via Ni-catalyzed thermal chemical vapour deposition and their violet-blue luminescent properties. *CrystEngComm* **2013**, *15*, 785–790. [CrossRef]

3. Hu, X.; Shao, C.W.; Wang, J.; Wang, H.; Cheng, J. Effects of residual radicals on compositional and structural stability of silicon nitride fibers. *J. Eur. Ceram. Soc.* **2017**, *37*, 4497–4503. [CrossRef]

4. Wu, J.M.; Zhang, X.Y.; Xu, J.; Gan, K.; Li, J.L.; Li, C.H.; Yang, J.L.; Shi, Y.S. Preparation of porous Si$_3$N$_4$ ceramics via tailoring solid loading of Si$_3$N$_4$ slurry and Si$_3$N$_4$ poly-hollow microsphere content. *J. Adv. Ceram.* **2015**, *4*, 260–266. [CrossRef]

5. Liu, X.Z.; Yi, X.M.; Guo, R.; Li, Q.D.; Nomura, T. Formation mechanisms of Si$_3$N$_4$ microstructures during silicon powder nitridation. *Ceram. Int.* **2017**, *43*, 16773–16779. [CrossRef]

6. Park, Y.J.; Park, M.J.; Kim, J.M.; Lee, J.W.; Ko, J.W.; Kim, H.D. Sintered reaction-bonded silicon nitrides with high thermal conductivity: The effect of the starting Si powder and Si$_3$N$_4$ diluents. *J. Eur. Ceram. Soc.* **2014**, *34*, 1105–1113. [CrossRef]

7. Strong, K.T.; Arreguin, S.A.; Bordia, R.K. Controlled atmosphere pyrolysis of polyureasilazane for tailored volume fraction Si$_3$N$_4$/SiC nanocomposites powders. *J. Eur. Ceram. Soc.* **2016**, *36*, 3663–3669. [CrossRef]

8. Sun, S.Y.; Wang, Q.; Ge, Y.Y.; Tian, Z.B.; Zhang, J.; Xie, Z.P. Synthesis of well-dispersed columnar Si$_3$N$_4$ using carbothermal reduction–nitridation method. *Powder Technol.* **2018**, *331*, 322–325. [CrossRef]

9. Karakuş, N.; Kurt, A.O.; Duran, C.; Öztürk, C.; Toplan, H.Ö. Sintering behaviour of silicon nitride powders produced by carbothermal reduction and nitridation. *Adv. Powder Technol.* **2013**, *24*, 697–702. [CrossRef]

10. Magnani, G.; Galvagno, S.; Sico, G.; Portofino, S.; Freda, C.; Burresi, E. Sintering and mechanical properties of β-SiC powder obtained from waste tires. *J. Adv. Ceram.* **2016**, *5*, 40–46. [CrossRef]

11. Yin, L.; Xu, Y.G.; Huang, Z.H.; Liu, Y.G.; Fang, M.H.; Liu, B.L. Synthesis of ZrN–Si$_3$N$_4$ composite powders from zircon and quartz by carbothermal reduction and nitridation. *Powder Technol.* **2013**, *246*, 677–681. [CrossRef]

12. Arik, H. Synthesis of Si$_3$N$_4$ by the carbo-thermal reduction and nitridation of diatomite. *J. Eur. Ceram. Soc.* **2003**, *23*, 2005–2014. [CrossRef]

13. Anggraini, L.; Natsume, Y.; Ameyama, K. Effect of particle shape on dispersion formation of harmonic microstructure of Si$_3$N$_4$-ZrO$_2$. *Mater. Sci. Forum* **2016**, *864*, 47–51. [CrossRef]

14. Hu, Z.L.; Zhu, T.B.; Wu, W.W.; Peng, Z.J.; Hu, F.; Xie, Z.P. Growth mechanism of α-Si$_3$N$_4$ submicron rods prepared from amorphous Si$_3$N$_4$ powders. *Ceram. Int.* **2018**, *44*, 22003–22007. [CrossRef]

15. Yu, J.J.; Guo, W.M.; Wei, W.X.; Lin, H.T.; Wang, C.Y. Fabrication and wear behaviors of graded Si$_3$N$_4$ ceramics by the combination of two-step sintering and β-Si$_3$N$_4$ seeds. *J. Eur. Ceram. Soc.* **2018**, *38*, 3457–3462. [CrossRef]

16. Huang, J.T.; Huang, Z.H.; Yi, S.; Liu, Y.G.; Fang, M.H.; Zhang, S.W. Fe-catalyzed growth of one-dimensional α-Si$_3$N$_4$ nanostructures and their cathodoluminescence properties. *Sci. Rep.* **2013**, *3*, 3504. [CrossRef]

17. Li, B.; Li, G.Q.; Chen, J.H.; Chen, H.Y.; Xing, X.M.; Hou, X.M.; Li, Y. Formation mechanism of elongated β-Si$_3$N$_4$ crystals in Fe-Si$_3$N$_4$ composite via flash combustion. *Ceram. Int.* **2018**, *44*, 9395–9400. [CrossRef]

18. Chen, K.; Huang, Z.H.; Liu, Y.G.; Fang, M.H.; Huang, J.T.; Xu, Y.G. Synthesis of β-Si$_3$N$_4$ powder from quartz via carbothermal reduction nitridion. *Powder Technol.* **2013**, *235*, 728–734. [CrossRef]

19. Dahal, N.; Chikan, V. Phase-controlled synthesis of iron silicide (Fe$_3$Si and FeSi$_2$) nanoparticles in solution. *Chem. Mater.* **2010**, *22*, 2892–2897. [CrossRef]

20. Ortega, A.; Alcalá, M.D.; Real, C. Carbothermal synthesis of silicon nitride (Si$_3$N$_4$): Kinetics and diffusion mechanism. *J. Mater. Process. Technol.* **2008**, *195*, 224–231. [CrossRef]

21. Li, J.; Shao, G.; Ma, Y.; Zhao, X.T.; Wang, H.L.; Zhang, R. Processing and properties of polycrystalline cubic boron nitride reinforced by SiC whiskers. *Int. J. Appl. Ceram. Technol.* **2019**, *16*, 32–38. [CrossRef]

22. Wang, Q.; Sun, S.Y.; Li, S.; Guo, Z.Y. Carbothermal synthesis of approximately spherical Si$_3$N$_4$ particles with homogeneous size distribution. *Ceram. Int.* **2018**, *44*, 22680–22685. [CrossRef]

23. Ji, H.P.; Huang, Z.H.; Chen, K.; Li, W.J.; Gao, Y.F.; Fang, M.H.; Liu, Y.G.; Wu, X.W. Synthesis of Si$_3$N$_4$ powder with tunable α/β-Si$_3$N$_4$ content from waste silica fume using carbothermal reduction nitridation. *Powder Technol.* **2014**, *252*, 51–55. [CrossRef]

24. Huang, J.T.; Miao, Y.P.; Zhang, M.; Feng, Z.J.; Hu, Z.H.; Li, X.B.; Luo, J.M. Hot-pressed sintered Ca-α-Sialon ceramics with grains from short prismatic to elongated morphology synthesized via carbothermal reduction and nitridation. *J. Alloy. Compd.* **2018**, *767*, 90–97. [CrossRef]

25. Li, X.M.; Li, R.; Zhu, X.T.; Zhou, Y.L.; Ren, G.N.; Zhang, L. Properties of large-sized porous Si$_3$N$_4$ ceramic tubes fabricated by carbothermal reduction of diatomite preforms. *Ceram. Int.* **2017**, *43*, 10559–10565. [CrossRef]

26. Charoo, M.S.; Wani, M.F. Friction and wear properties of nano-Si$_3$N$_4$/nano-SiC composite under nanolubricated conditions. *J. Adv. Ceram.* **2016**, *5*, 145–152. [CrossRef]

27. Li, X.L.; Wang, J.; Ji, H.M.; Xu, X.W. Catalytic Effect and Mechanism of Fe$_2$O$_3$ on Synthesis of Si$_2$N$_2$O by Carbothermal Reduction and Nitridation of SiO$_2$. *Aerosp. Mater. Technol.* **2012**, *2*, 95–98.

28. Boyer, S.M.; Moulson, A.J. A mechanism for the nitridation of Fe-contaminated silicon. *J. Mater. Sci.* **1978**, *13*, 1637–1646. [CrossRef]

29. Guo, W.M.; Yu, J.J.; Xiong, M.; Wu, S.H.; Lin, H.T. High-toughness Lu$_2$O$_3$-doped Si$_3$N$_4$ ceramics by seeding. *Ceram. Int.* **2016**, *42*, 6495–6499. [CrossRef]

30. Wang, B.; Yang, J.; Guo, R. Microstructure and property enhancement of silicon nitride-barium aluminum silicate composites with β-Si$_3$N$_4$ seed addition. *J. Mater. Sci.* **2009**, *44*, 1351–1356. [CrossRef]

31. Marin, E.; Adachi, T.; Boschetto, F. Biological response of human osteosarcoma cells to Si$_3$N$_4$-doped Bioglasses. *Mater. Des.* **2018**, *159*, 79–89. [CrossRef]

32. Jun, Y.S.; Kim, D.; Neil, C.W. Heterogeneous nucleation and growth of nanoparticles at environmental interfaces. *Accounts Chem. Res.* **2016**, *49*, 1681–1690. [CrossRef] [PubMed]

33. Topateş, G. Direct production of Si$_3$N$_4$ foams by carbothermal reduction and nitridation of SiO$_2$. *Ceram. Int.* **2018**, *44*, 20545–20550. [CrossRef]

34. Karakus, N.; Kurt, A.O.; Toplan, H.Ö. Synthesizing high α-phase Si$_3$N$_4$ powders containing sintering additives. *Ceram. Int.* **2009**, *35*, 2381–2385. [CrossRef]

35. Bandyopadhyay, S.; Mukerji, J. Reaction sequences in the synthesis of silicon nitride from quartz. *Ceram. Int.* **1991**, *17*, 171–179. [CrossRef]

36. Wang, F.; Qin, X.F.; Yang, L.X. Synthesis and photoluminescence of Si$_3$N$_4$ nanowires from La/SiO$_2$ composites and Si powders. *Ceram. Int.* **2015**, *41*, 1505–1510. [CrossRef]

37. Huang, J.T.; Zhang, S.W.; Huang, Z.H. Catalyst-assisted synthesis and growth mechanism of ultra-long single crystal α-Si$_3$N$_4$ nanobelts with strong violet-blue luminescent properties. *CrystEngComm* **2012**, *14*, 7301–7305. [CrossRef]

38. Robertson, J.; Powell, M.J. Gap states in silicon nitride. *Appl. Phys. Lett.* **1984**, *44*, 415–417. [CrossRef]

39. Xiong, L.; Dai, J.H.; Song, Y. Effects of doping on photoelectrical properties of one-dimensional α-Si$_3$N$_4$ nanomaterials: A first-principles study. *Phys. B Condens. Matter* **2018**, *550*, 32–38. [CrossRef]